Research Square

Preprints are preliminary reports that have not undergone peer review.
They should not be considered conclusive, used to inform clinical practice,
or referenced by the media as validated information.

Predicting Intergranular Corrosion Penetration Depth in Accelerated Testing using Machine Learning

David Montes de Oca Zapiain

dmonte@sandia.gov

Sandia National Laboratories

Christoph Altenbach

German Aerospace Center (DLR)

Laura Kopruch

RWTH Aachen University

Aditya Venkatraman

Sandia National Laboratories

Ryan M. Katona

Sandia National Laboratories

Daniela Zander

German Aerospace Center (DLR)

Article

Keywords: Aluminum Alloys, 6000 Series Aluminum Alloys, Knowledge Extraction

Posted Date: August 27th, 2026

DOI: https://doi.org/10.21203/rs.3.rs-10744979/v1

License: This work is licensed under a Creative Commons Attribution 4.0 International License.
Read Full License

Additional Declarations: No competing interests reported.

Predicting Intergranular Corrosion Penetration Depth in Accelerated Testing using Machine Learning

David Montes de Oca Zapiain[a,*], Christoph Altenbach[b], Laura Kopruch[c], Aditya Venkatraman[a], Ryan M. Katona[a], Daniela Zander[b,c]

[a] *Sandia National Laboratories, 1515 Eubank Blvd SE, Albuquerque, 87123, NM, United States of America*

[b] *German Aerospace Center (DLR), Institute for Frontier Materials on Earth and in Space, Linder Höhe, Cologne, 51147, NW, Germany*

[c] *RWTH Aachen University, Chair of Corrosion and Corrosion Protection, Intzestr. 5, Aachen, 52072, NW, Germany*

Abstract

Aluminum (Al) 6000 series alloys are relevant in automotive applications due to great strength, excellent machinability, formability, as well as good weldability. Nevertheless, aluminum alloys are susceptible to intergranular corrosion (IGC) making it crucial to determine the relationship that exists between the alloy composition and manufacturing parameters to the corresponding rate and magnitude of IGC observed. The large number of parameters that affect this behavior requires the development of a more robust framework. In this work, a probabilistic model is leverage to establish an accurate linkage between a set of input parameters (*e.g.*, alloying content, heat treatment, *etc.*) and the resultant IGC performance (*i.e.*, penetration depth) of multiple Al 6000 series alloys. The model extracts usable knowledge from a curated database comprised of 128 individual experimental results. The developed framework

*Corresponding author.

Email address: dmonte@sandia.gov (David Montes de Oca Zapiain)

August 17, 2026

and established models are further validated by predicting the penetration depth of six new/unseen alloys.

Keywords:

Aluminum Alloys, 6000 Series Aluminum Alloys, Knowledge Extraction

---

Introduction

The unique combination of properties from Al-Mg-Si(-Cu) alloys (6000 series) such as specific strength, excellent machinability, formability and weldability, make them relevant for automotive applications [1]. 6000 series aluminum are commonly used as sheet materials in the outer skin, as well as for extrusions in structural parts and screws [1, 2, 3]. While these alloys exhibit adequate corrosion resistance, particularly with regards to stress corrosion cracking and hydrogen embrittlement [4, 5], they can be susceptible to intergranular corrosion (IGC). IGC propagates rapidly, is difficult to detect with line of site methods, and leads to reduced mechanical load capacity due to the formation of crack initiation sites [6, 7].

The IGC susceptibility is determined not only by the operating environment, but also by multiple parameters such as the chemical composition, casting and solidification parameters, and the thermomechanical history [2, 4, 8, 9, 10]. For this reason, it is crucial to determine the influence of the various parameters in terms of rate and magnitude of IGC observed in Al-Mg-Si(-Cu) alloys.

Experimental efforts have observed various trends in the IGC behavior of 6000 series aluminum alloys. For example, IGC susceptibility has been correlated to multiple distinct mechanisms, including grain boundary precipitation (Q-$Al_5Cu_2Mg_8Si_6$, β-Mg_2Si) [2, 10, 11, 12, 13, 14], precipitate-free zones and element depletion zones

(Mg, Si and Cu) [15, 16, 17, 4, 13, 18, 14], as well as element enrichment (Cu and/or Si) [10, 11, 15, 19, 20]. Besides the direct initiation at susceptible grain boundaries, IGC can also be initiated by the exposure of susceptible grain boundaries through pitting corrosion, which results from the local dissolution of the surrounding aluminum matrix caused by cathodic oxygen reduction reaction (ORR) at intermetallic particles, such as Fe-rich phases [21, 22].

Experiments have also enabled the development of fundamental understanding between the effect that different alloying elements have on the resultant IGC susceptibility [23, 24]. For example, it has been reported that the Mg to Si ratio is a determining factor in Cu-lean aluminum alloy's susceptibility to IGC [11, 19]. This can be attributed to the presence of excess Si that is not bound within the precipitates. This excess Si has the tendency to segregate to the grain boundaries, resulting in an anodic behavior of the Si-depleted precipitate-free zone (PFZ) adjacent to the Si-enriched grain boundaries [11, 19]. However, Cu-lean alloys are mostly reported as resistant to IGC [10], while Cu-rich alloys are susceptible to IGC even after short-term artificial aging [3, 10]. In Cu-rich alloys, the IGC susceptibility has been related primarily to the Cu content and, secondarily, to the Mg/Si ratio, whereby excess Mg can improve the IGC resistance [23].

Similar relationships have also been observed between the severity of IGC and the heat treatment to which the alloy was exposed. Conditions such as T6 (peak-aged condition using artificial aging), and T4 (solution annealed, quenched and naturally aged), have a significant effect on the observed IGC behavior [3, 2]. The effect of overaging and underaging on the resultant behavior has also been analyzed [3, 17].

Previous work showed that the susceptibility of Cu-containing alloys to IGC in the "underaged" and T6 condition is explained by the formation of a Cu nanofilm at the grain boundary, which has a cathodic effect on the surrounding Cu-depleted PFZ [12, 16]. It has also been mentioned that with increasing aging to the over-aged state, the copper diffuses into the Q-phases at the grain boundary, whereby galvanic coupling of the Q-phase with the Cu-depleted PFZ becomes the dominant mechanism [10, 12, 20, 25]. Moreover, it has been shown that dispersoid-forming elements such as Cr, Mn, Zr, Sc or V have a significant impact on the grain aspect ratio of the Al-Mg-Si(-Cu) alloys [1, 26, 27, 28]. These elements effectively suppress recrystallization and promote the formation of subgrain boundaries during the forming process. Hence, the segregation of Mg, Si and Cu is reduced due to a greater number of potential nucleation sites. Consequently, less continuous coverage of high-angle grain boundaries with precipitates is expected, leading to a less predetermined corrosion path.

It can be see that experimental analysis is critical for establishing insights and developing fundamental understanding between the inputs and outputs for IGC. Nevertheless, these insights require many experiments that are complex and capital intensive. Consequently, the cost and time required to perform these experiments throttles the number of experiments that can be performed. Therefore, in cases when multiple variables are evaluated, experiments yield insights and correlations that can be leveraged as heuristic design rules, aiding in the selection of a material, but fail to provide an estimation or prediction of the extent of IGC that can occur. Thus, in order to evaluate the specific performance of an alloy, a variety of standardized accel-

erated corrosion tests must be performed [29]. Evaluating the performance of each alloy using experimental tests, even if accelerated, represents an additional challenge as the results of these tests are not often comparable to the end application [30, 21]. Furthermore, given the open parameterization of certain standards, a broad range of input parameters can satisfy the requirements [29, 30, 31]. This results in variability of the IGC susceptibility of an alloy and can complicate the comparison and transfer of results between different laboratories or testing procedures. Consequently, a new iteration of experiments is required each time a new alloy or parameter needs to be evaluated. Therefore, a more robust and efficient framework for assessing the IGC performance of alloys is crucial.

Machine learning (ML) is a viable solution for establishing the desired framework given its ability to establish accurate and robust linkages between inputs and outputs that exhibit complex and non-linear behavior [32]. Futhermore, it has been successfully leveraged for corrosion characterization and prediction in the past [33, 34, 35, 36].

Li et al. [37] and Feng et al. [38] demonstrate that ML can be successfully applied for providing a prediction of the IGC performance of an Al-Mg-Si alloy (*i.e.*, penetration depth), and that the results can be further utilized as a design tool. Sheik et al. [39] leveraged ML to predict the degree of sensitization (DOS) from a set of experimentally obtained measurements, while Falaakh et al. [40] extracted knowledge from a database of crack growth rates. In general, ML models can extract usable knowledge from previously obtained IGC results. Nevertheless, existing implementations relied mostly on deterministic models for the predictions and do

not account for uncertainty quantification. As Falaakh et al. [40] point out, this capability can be incorporated by employing boosting (*i.e.*, model ensembling [41]). As a result, a systematic knowledge extraction protocol capable of providing not only a prediction but rather a distribution of predictions for a given set of inputs for the IGC performance of Al-Mg-Si(-Cu) alloys still needs to be developed/implemented.

In this work, the aforementioned gap is addressed by leveraging probabilistic models to establish an accurate linkage between a set of input parameters (*e.g.*, alloying content, heat treatment) and the resultant IGC performance (*i.e.*, penetration depth) of multiple Al-Mg-Si(-Cu) alloys. To achieve this, a database of the penetration depth of 128 individual tests for multiple alloys was curated from previously published work [2, 3, 4, 8, 9, 29, 30, 42]. Subsequently, following previous successes [43], Gaussian Processes (GPs), which are a type of probabilistic models [44], were utilized to connect the set of inputs to the obtained penetration depth. Finally, the created model was validated by using it to predict the maximum penetration depth of six new alloys.

Results

Experimental Analysis

A database of results from previously published work was curated [2, 3, 4, 29, 30, 42] that comprised of distinct variables, such as alloying content and heat treatment, and the resultant penetration depth for Al-Mg-Si(-Cu) alloys. The heat treatment conditions considered are T4 and T6, as well as a condition that simulates the heat exposure during the painting stage in automotive manufacturing, referred to as bake

hardening (BH). The latter can be regarded as an underaged condition. Further variables that were considered result from the standardized testing procedure according to ISO 11846 method B [31]. Overall, the database contains 128 separate experiments, and the specific variables analyzed with the experiments are detailed in Table 1.

Table 1: Experimental variables and their corresponding types.

Parameter	**Type of variable**
Cu [wt.%]	Continuous (numeric)
Mg [wt.%]	Continuous (numeric)
Si [wt.%]	Continuous (numeric)
HT condition	Categorical
Volume/Surface Area [ml/cm^2]	Continuous (numeric)
$T_{\text{electrolyte}}$ [°C]	Continuous (numeric)
t [min]	Continuous (numeric)
T [°C]	Continuous (numeric)
HNO_3 [ml/l]	Continuous (numeric)
HF [ml/l]	Continuous (numeric)
NaOH conc.	Continuous (numeric)
Storage Time [d]	Continuous (numeric)

A preliminary analysis of the database was performed by plotting the values of the penetration depth against the values of the distinct variables recorded and colored by heat treatment, shown in Figure 1. While some qualitative trends exist in the scatter plots (Figure 1), it is quite complicated to extract precise trends. For example, from Figure 1(a) a general trend of increasing penetration depths as % of Cu increases can be observed. However, the trend is limited since a broad dispersion of penetration depth values is observed at the same Cu content. In other cases (Figure 1(g)) a trend is not apparent as similar penetration depths are associated with distinct values of temperature.

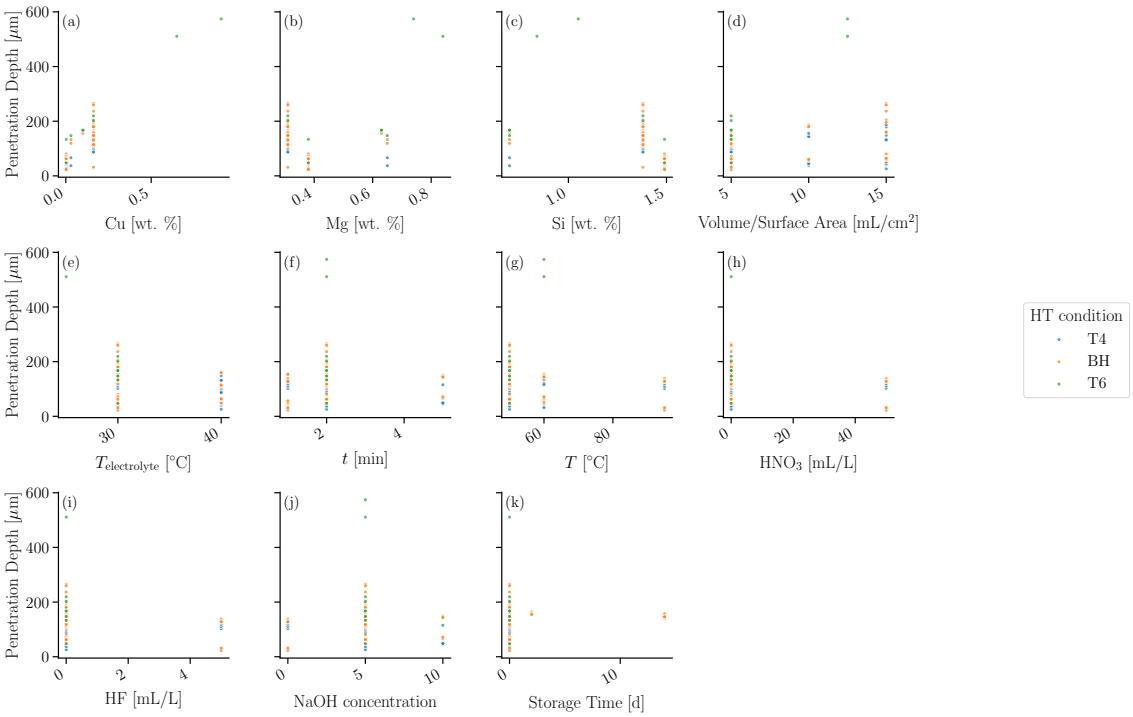


Figure 1: Scatter plots for each of the distinct input variables vs. the penetration depth for the compiled experimental results colored by heat treatment: T4 (solution annealed, quenched and naturally aged); T6 (peak aged), BH (bake hardened/ underaged.

Although trends are not immediately visible, this does not imply the absence of a relationship between the distinct variables and the penetration depth. It potentially indicates that the relationship is complex, given the high-dimensionality of the space, and most likely non-linear. Consequently, conventional analysis is limited in extracting qualitative insights from the vast amount of information present. This underscores the importance of implementing ML-based techniques for building linkages between the inputs and outputs.

Knowledge Extraction using Gaussian Processes

A computationally efficient linkage between the input parameters and the resultant IGC performance of the collated experimental data using Gaussian Processes Regression (GPR) models [44] was created. In this work, the set of inputs contain a mixture of categorical and continuous values as detailed in Table 1. The output corresponds to the penetration depth in μm. Following standard practice, feature engineering was performed to the inputs and outputs. Categorical variables were transformed using a One-Hot Encoder and then subsequently normalized to the $[0, 1]$ domain. In a similar manner, the output values were normalized to the $[0, 1]$ domain. These transformations and normalizations were applied using SciKit Learn[45].

The experimental data has inherent uncertainty that is captured by using a mean penetration depth and its corresponding standard deviation of five measurements. Naturally, the standard deviations of the distinct captured measurements are not homogeneous. To account for the variability of the uncertainty across the distinct experiments, two distinct GPR-based models were used: one that predicts the penetration depth and the second that predicts the estimated variability associated with that prediction.

As a result, the GPR-based model that predicts the penetration depth also provides an associated variability but that variability is solely related to the model itself (*i.e.*, epistemic uncertainty) while the GPR-based model that provides the estimated variability accounts for the variability that is observed directly from the experiments (*i.e.*, the aleatoric). This decomposition captures not only the effect the distinct

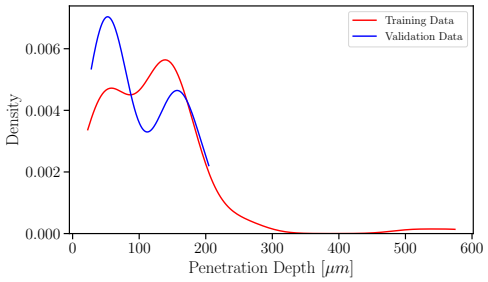


Figure 2: Probability density distribution of the recorded penetration depth in μm for the training and testing datasets

inputs have on the outputs but also on their corresponding variability [46, 47].

To ensure that the models are capable to generalize and are not overfitted, the Training Data contained 80% of the data available, randomly sampled, while the remaining 20% was used as the Validation Data. Figure 2 shows the penetration depth for the training and the validation sets. To facilitate interpretability, all the results are reported in the un-normalized domain. Figure 2 further shows that the training data encompasses the validation data and that the validation data is distinct from the training data. This indicates that the validation data can be utilized to evaluate the performance of the model to predict new/unseen inputs.

The GPR-based model for predicting penetration depth uses a Matérn-5/2 kernel and has a zero mean function [44]. The parameters for this model were fitted by maximizing the log marginal likelihood [44]. To enhance the model fitting process, a multi-start optimization strategy was employed. This strategy performs multiple random initializations of the model parameter values that are then optimized using maximum likelihood estimation (MLE) and proceeds to select the best performing model of all the performed initializations, which is the one that exhibits the lowest

negative log marginal likelihood. For this work 50 distinct initializations were performed. *GPflow* [48] was used for performing the described model-fitting protocol.

A similar process for fitting the GPR-based model that predicts the experimental variability was used. Note that the output of this second model is the experimental variance, which was obtained by taking the square of the reported experimental standard deviation denoted by σ_{exp}. The experimental variance is thus denoted by σ^2_{exp}. To enable a better model fitting process, the range of observed variance was normalized to the $[0, 1]$ domain, which we denote as $\hat{\sigma}^2_{exp}$. To ensure that the variance is always positive following transformation was applied:

$$\hat{\sigma}^2_{exp_t} = \log\left(1 + \hat{\sigma}^2_{exp}\right). \tag{1}$$

As a result, the second model was fitted on the transformed variance denoted by Eq. 1. A Rational Quadratic kernel with a constant mean function was used for the experimental variability GPR-based model. Similarly to the penetration depth GPR-based model, the uncertainty GPR model was fitted using MLE and a multi-start optimization strategy with 50 distinct initializations using *GPflow*. The total variance was calculated by adding the prediction of experimental variability GPR-based model to the uncertainty prediction obtained by the penetration depth GPR-based model as follows:

$$\sigma^2_{\text{total}}(x) = s^2_{\text{GP}}(x) + \hat{\sigma}^2_{\text{exp}}(x), \tag{2}$$

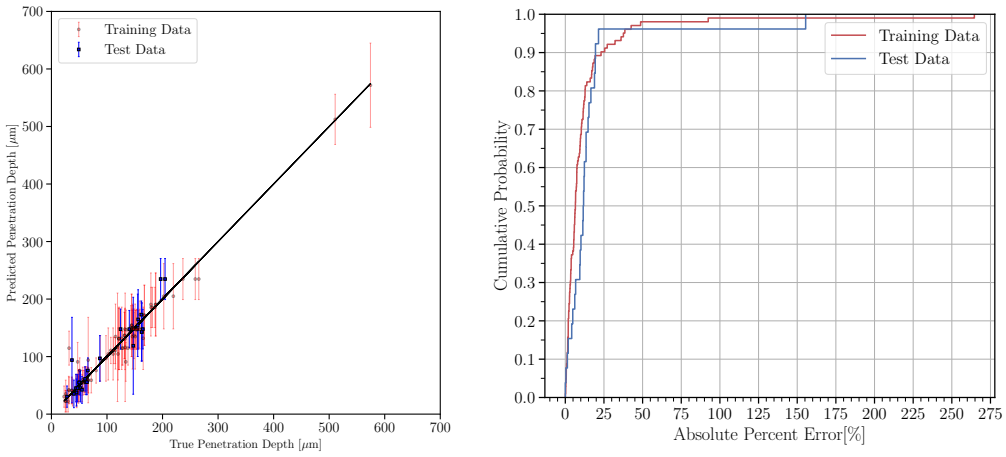
where $s^2_{\text{GP}}(x)$ is the variance predicted by the penetration-depth GP. Also, recall

that the variability GPR-based model was trained on a scaled and log-transformed variance target (cf. Eq. 1). Therefore, before adding $\hat{\sigma}^2_{exp}$ to the variance predicted by the penetration-depth GP, $\hat{\sigma}^2_{exp_t}$ was inverse-transformed and un-normalized.

The plots in Figure 3 showcase the performance of the developed computationally efficient linkage established the two GPR-based models. Specifically, Figure 3(a) shows the true vs. predicted scatter plot of the established linkage. The scatter points correspond to the mean value of the penetration depth predicted using the penetration depth GPR-based model and the error bands correspond to two standard deviations of the total variance, which were obtained by taking the square root of $\sigma^2_{\text{total}}(x)$. The predicted values lie close to the diagonal line, indicating that the predictions are accurate. A majority of the points on the diagonal line are within two standard deviations of the total predicted variance. Additionally, Figure 3(b) shows the cumulative distribution of the absolute percent error and roughly 90% of the predictions for the training and test data have an error less than 25%. Both of these plots showcase the accuracy of the fitted models. Finally, the mean absolute percent error (MAPE) is 12.3% for the training data and 16.2% for the test data, these numbers show that, despite a small overfit, the model is overall capable of generalizing to new/unseen scenarios. This observation is also supported from the similar behavior of the model in the two distinct sets showcased in Figures 3(a) and (b).

Predicting the Penetration Depth of New Dataset using the Extracted Knowledge

To further demonstrate the validity and efficacy of the trained models, nine new experiments were performed and the trained models were used to predict their corre-



(a) (b)

Figure 3: (a)Scatter plot of the predicted vs. true penetration depth values (in μm) with two standard deviations as the error bars. (b) Cumulative distribution of the Absolute Percent error for the Training and the Testing datasets.

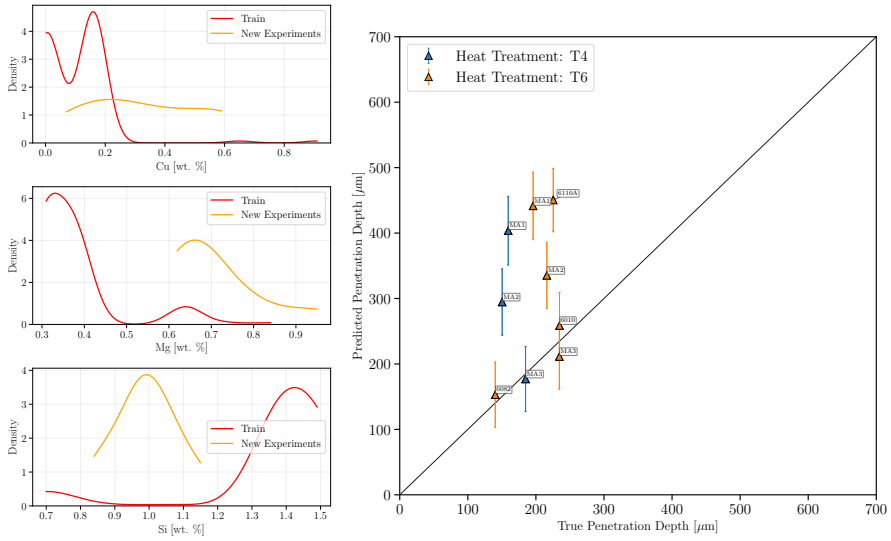
sponding penetration depth. The experiments evaluated the performance of six new alloys.

The first three new experiments are Al-Mg-Si(-Cu) model alloys with a decreasing amount of copper. The copper weight percentage of the model alloys labeled MA1, MA2 and MA3 are 0.59 wt. % Cu ,0.35 wt. % Cu and 0.16 wt. % Cu, respectively. These alloys are denoted with triangles in Figure 7(a). The remaining three alloys investigated are 6082, 6110A and 6010 and their specific composition is highlighted in Figure 7(a) with labeled triangles as well. It is pointed out that the effect of the heat treatment was evaluated on the MA's by performing experiments on the material in T4 and T6 condition. Therefore, a total of nine new experiments were performed.

Figure 4(a) shows the composition details of the new alloys evaluated in the

experiments using probability density distribution plots. From Figure 4(a), it is clear that the new experiments are evaluating a distinct area of composition space. Although the compositions are not included in the training set, the new alloys are mostly comprised by the limits of the training data as only a tiny fraction of the data explores a Mg weight percentage that is outside of the training regime. Therefore, under these conditions the model will be mostly interpolating.

Figure 4(b) showcases the performance of the model on the new alloys plotting the value predicted with the model against the true penetration depth value obtained after performing the experiment. As illustrated (4(b)), the model has notable accuracy in predicting new experimental values for 6082, MA3 (for both heat treatments) and 6010 to the fitted line. However, in other cases, the model over-predicted the penetration depth to a significant extent, regardless of the heat treatment condition.



(a) (b)

Figure 4: (a) Scatter plot of the predicted vs. true penetration depth values (in μm) with two standard deviations as the error bars for the New Experiments dataset colored by heat treatment. (b) Probability density distribution plots of the distinct alloying components for the Training Data and the New Experiments dataset.

For predictions related to corrosion damage, an over-prediction from the model is preferred given this leads to over-engineering and over-estimation of damage rather than early failure damage, which can be catastrophic. Despite this, the fact remains that for some alloys and their corresponding heat treatment conditions, the model estimated a drastically higher penetration depth than recorded from the experiment.

Analyzing the composition of the new alloys, it is noticed that the alloys for which the model over-predicted have a copper content that is greater than 0.22 wt. % Cu. This information is obtained from the legend key on Figure 4(b) and the composition chart shown in Figure 7(a). Additionally, as displayed in Figure 1(a) the higher copper content typically corresponds to higher values of penetration depth. Therefore, the model qualitatively behaving as expected given that it is displaying the trend captured by the training data. However, the experiments performed on the new alloys did not exhibit that trend. As noted in Table 2, the MA's have similar Mg/Si ratios but decreasing Cu content with MA1 having the highest Cu and MA3 having the lowest Cu content. Experimentally, all MAs had a similar true penetration depth (Figure 4(b)). This is also noted in 6110A and MA1 in Figure 4(b) as both alloys contained a Cu content great then 0.57 wt. %. Therefore, it is likely that another mechanism or cause is responsible for the decrease in performance.

In order to uncover this, the microstructure of the alloys was analyzed. Figure 5 shows the Barker etched light microscopy images of the grain structure of the model alloys. Electrolytic Barker etching is a process that reveals the grain structure of aluminum alloys under a polarized light microscope. During the Barker etching process, a layer of oxide is formed, the thickness of which varies depending on the grain orien-

tation [49]. This variation in thickness alters the reflectivity for certain wavelengths under polarized light, thereby enabling the distinction of individual grains. Images have been taken from the material in T4 condition in each sheet direction to gain a more comprehensive understanding of the rolling texture of the sheet material. The additional artificial heat treatment to the T6 condition will not change the grain size, since the temperature is below the recrystallization temperature of the alloys [9, 50]. Thus, only the T4 condition was analyzed. As shown in Figure 5, the grains of the model alloys are elongated in rolling direction (L). The elongation increases with the Cu content (*i.e.*, MA1 has more elongated grains than MA3). Simultaneously, the grains become narrower in the short transverse (ST). For 6010 and 6082 the model prediction demonstrates accurate predicted penetration depth. It is noted that these alloys exhibited a maximum content of 0.22 wt. %Cu. However, for 6110A (0.57 wt. %Cu), the deviation is found to be significant and is similar in performance to MA1. It can also be observed from Figure 5 that the grains of the 6110A are elongated in rolling direction (L).

As a result, in the present study, systems that have only slightly elongated grains or are more equiaxial (MA3, 6082, and 6010; Figure 5) are correctly predicted by the GP model (Figure 4). However, when more elongated grains are present (MA2, MA1, and 6110A; Figure 5) the GP model over-predicts damage (Figure 4).

In addition to the distinct grain structure and size, the corrosion mechanism is fundamentally different in some of the new alloys. Figure 6(a) and (b) show representative light microscopy images of the corrosion morphology of the model alloys in T4 and T6 heat treatments, respectively. In Figure 6(a), the T4 condition

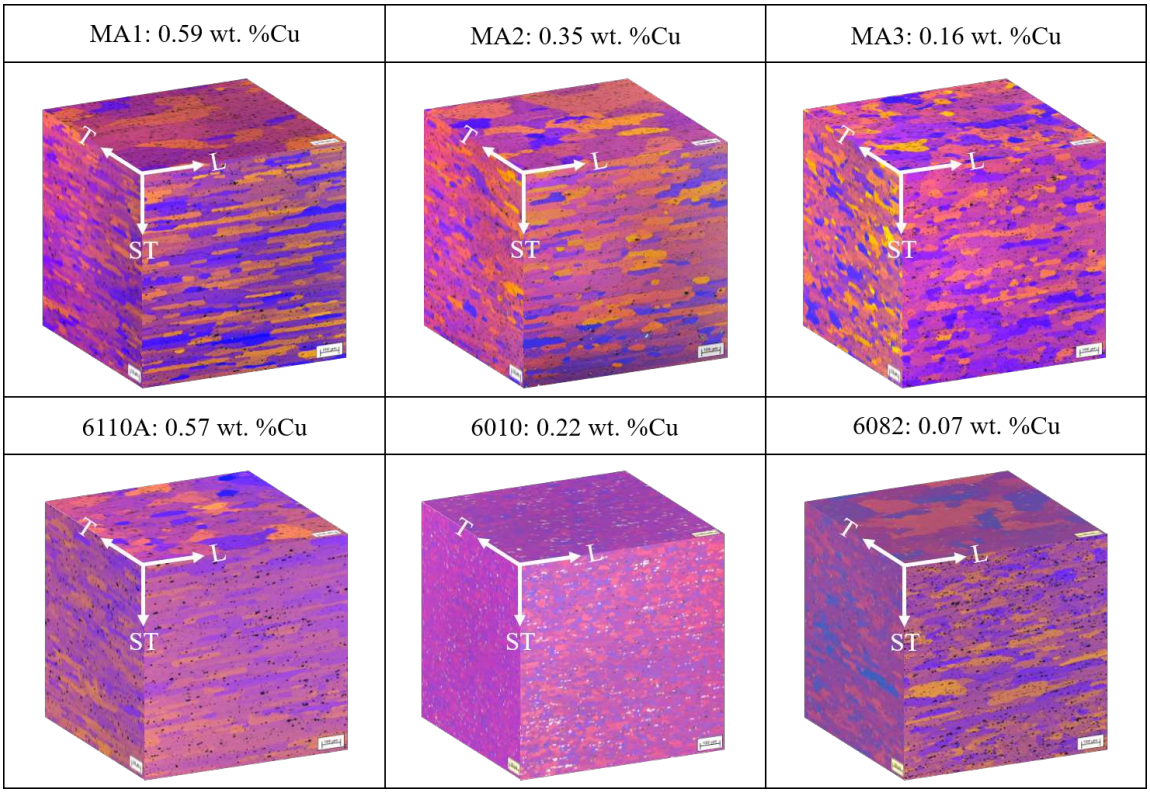
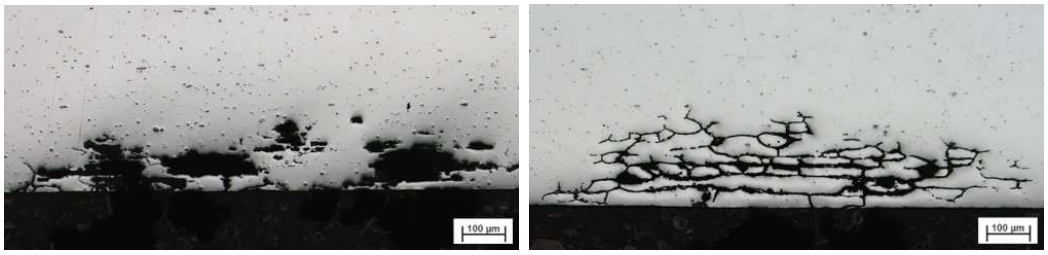


Figure 5: Barker etched light microscopy images of the grain structure of the MA's (MA1-MA3) evaluated with the new experiments.

exhibits pitting corrosion while the T6 condition (Figure 6(b)) exhibits IGC. With artificial aging the mechanism switches from pitting to IGC.

It is important to acknowledge that the curated database solely contained experimental results relating to IGC. Thus, the model has not been exposed, nor trained to predict the damage caused by pitting corrosion. This represents another reason for the drastic reduction in accuracy from the previously trained model. It cannot be expected for the model to be able to generalize to new mechanisms if the model has not been trained on such examples.



(a) (b)

Figure 6: Representative light microscopy images (MA3) of the corrosion morphology in (a) T4 and (b) T6 condition, showing a switch in corrosion mechanism from pitting towards IGC with artificial aging for the MA's.

Discussion

The presented results demonstrate that GPR-based models are capable of distilling usable knowledge from previously obtained experimental results. Additionally, the probabilistic nature of GPR allowed for an adequate treatment of the variability by accounting for the epistemic uncertainty as well as the aleatoric uncertainty. This capability is considered to be of significant value, since it can later be adequately leveraged to guide where to perform other experiments. The calibrated uncertainty can be applied as a criterion to determine the necessity for new experimentation. Thus, enabling a data-driven procurement of knowledge.

The results shown also highlighted that the distilled knowledge was capable of being generalized to new/unseen alloys as the trained model was able of providing accurate estimations of the penetration depth for some of the new model alloys analyzed in this work. It should be noted that the results of the model also indicated that it was not possible to provide accurate predictions for all of the alloys. Nevertheless, the decrease in performance and accuracy of the prediction was not caused by the GPR-based model itself.

The discrepancy between the behavior of the new alloys from the behavior recorded in the compiled and curated database was caused by the fact that the new alloys exhibited distinct microstructures (Figure 5). Especially, since IGC occurs mostly along the high angle grain boundaries as stated by Lervik et al. [51], the texture with elongated grains results in longer total path length for a smaller penetration depth towards the center of the sample. Therefore, the smaller penetration depth can be correlated to the elongated grains. Having said this, the trained model is unable

to account for this critical parameters given the fact that the curated experimental database of results did not provide (or did not record) details regarding the grain structure at the microscale.

Additionally, it was observed that some cases of over-prediction of penetration depth by the model were cases that exhibited pitting corrosion. Pitting corrosion is a fundamentally different mechanism to IGC, which was observed in the database. This is clearly demonstrated in Figure 6, which shows that pitting corrosion occurred in these cases, rather than the IGC behavior that was captured by the curated database. Pitting in Al-alloys occurs at (or at the interfaces of) second phase particles - where the protective passive film is different [52, 53]. Further, the galvanic coupling between cathodic intermetallic particles and the matrix, whereby the potential difference causes the surrounding matrix to dissolve leading to pitting [2, 21]. In contrast, the corrosion path follows the grain boundaries in the T6 condition due to galvanic coupling of the microstructural features of the grain boundaries, such as grain boundary precipitates [2, 10, 11, 12, 13, 14] or element enrichment [10, 11, 15, 19, 20] with the PFZ and/or SDZ [15, 16, 17, 4, 13, 18, 14]. The exact mechanisms remain highly dependent on the alloy composition, especially on contents of Mg, Si and Cu [24], or the exact thermomechanical history [10].

Despite the switch from pitting for the T4 condition to IGC for the T6 condition, the model still over predicts the IGC conditions. This further reiterates the importance of microstructure when considering IGC of aluminum alloys. The role of microstructure has been explored in many alloy systems [54]. For aluminum alloys, there is conflicting information in literature on the influence of grain size on the

resulting corrosion rate. The effect of grain refinement to be considered as purely a "structural" change is an oversimplification in the context of aluminum systems [54].

Thus, the decrease in accuracy and performance of the developed framework is caused by the fact that the trained model needs to incorporate adequately details regarding the microstructure and relevant physics in order to capture pitting corrosion, as well as taking into account the path length and branching of the IGC corrosion attack.

To improve model predictions, new features should be suitably incorporated into the input domain such as details regarding the microstructure. These new features need to sufficiently capture relevant information of the underlying grain orientation, grain structure as well as the morphology (*i.e.*, grain shape and size) of the grains in order to enhance the predictions and train a microstructure-aware surrogate model. This initially involves extensive microstructural analysis, but offers the potential to provide missing information about the manufacturing process into perspective in the future. Successfully predicting uncertainties also makes it possible to design an appropriate experimental design in the future as well as serve as a foundation for data collection in self-driving labs. Nevertheless, it is important to recognize that overall the developed framework successfully enabled for the extraction of usable knowledge and, most importantly, it enabled the capability to utilize such knowledge effectively and efficiently for new/unseen alloys.

Methods

Experimental Details

For the development of a prediction tool for the penetration depth of intergranular corrosion based on a machine learning approach, the penetration depths of the alloys shown in Tab. 2, which were previously published, were considered. With the exception of alloy AA6056 (wire material with diameters of either 10.25 mm or 8 mm [2, 13, 42, 4, 3]), these are sheet materials with thicknesses of approximately 1 mm [29, 30]. The selected sheet and wire samples exhibited predominantly equiaxial grain morphologies of similar sizes. The heat treatment conditions considered can be designated as either solution annealed and quenched (T4), bake-hardened (BH) and peak-aged (T6). As a blind test, three industrially produced and heat-treated model alloys with varying Cu contents are investigated in the T4 and T6 condition with a sheet thickness of 2 mm. Furthermore, results from sheet materials with a thickness of approximately 1 mm were considered for blind testing [8, 9]. The relevant contents of the main alloying elements Mg, Si and Cu can also be found in Tab. 2. As with previous publications, the exact heat treatment conditions are subject to confidentiality and can therefore not be made available here. The alloys used for model development, training and the blind test are shown in Fig. 7 for classification within the 6000 series with their Mg/Si vs. Cu and Mg vs. Si contents. The blue boxes indicate the chemical composition window of the alloys in the area of interest. Thee alloy designations have been carried over from the respective reference to the corresponding data points, and that some data points may deviate from the standard alloy specification given in [55]. This applies to the alloy composition of 6014,

Table 2: Chemical composition of the main alloying elements of 6000 series materials considered for the machine learning approach in wt. %.

Alloy	**Mg**	**Si**	**Cu**	**Ref.**
AA6016-High Cu	0.31	1.38	0.162	[29, 30]
AA6016-Low Cu	0.38	1.49	0.002	[29, 30]
AA6014-High Cu	0.63	0.7	0.1	[30]
AA6014-Low Cu	0.65	0.7	0.03	[30]
AA6056-High Cu	0.74	1.05	0.91	[2, 42]
AA6056-Low Cu	0.84	0.84	0.65	[3, 4]
AA6010	0.95	1.15	0.22	[8, 9]
AA6110A	0.73	0.84	0.57	[9]
AA6082	0.81	0.89	0.07	[9]
MA1	0.68	1.06	0.59	
MA2	0.65	0.99	0.35	
MA3	0.62	0.97	0.16	

visible in Fig. 7 b). Furthermore, the stoichiometric composition limit of the Mg_2Si equilibrium phase is shown, which marks the transition to the undesirable excess Mg region [56, 57]. The dashed lines indicate the limits of a positive intermediate storage effect [58] and Mg_2Si solubility [57].

The IGC susceptibility of the model alloys is tested according to EN ISO 11846 method B [31], taking into account the standard test parameters defined by Zander et al..[29] The samples are first cut to a size of 29 mm x 49 mm and then pickled in 5 % NaOH solution at 50 °C for 2 min, followed by immersion in an aqueous solution of 30 g/l NaCl and 10 ml concentrated HCl (37 %) for 24 h. The surface-to-volume ratio is set to 5 ml/cm^2 in order to equalize the influence of the sample size, which may be between 4 and 20 ml/cm^2 according to EN ISO 11846 method B. The samples are immersed into beakers using a chemical-resistant, non-conductive plastic clamp and a nylon thread so that the surface is almost completely wetted. The beakers are

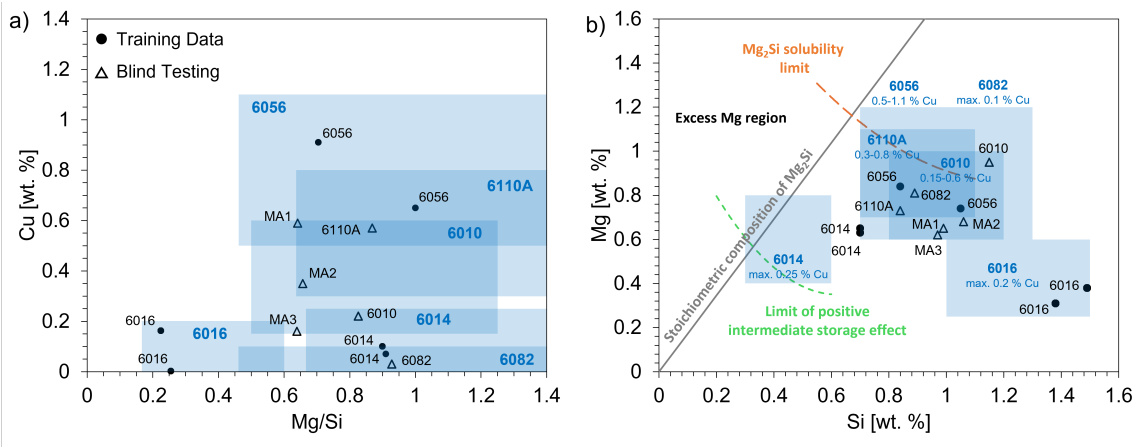


Figure 7: Classification of used alloys for model development and blind testing related to (a) Mg/Si vs. Cu and (b) Si vs. Mg content within the 6000 series designation system [29, 30, 2, 3, 8, 9]. Blue boxes indicate the chemical composition range according to the specification in the teal sheets [55]. The model alloys are marked as MA1-MA3.

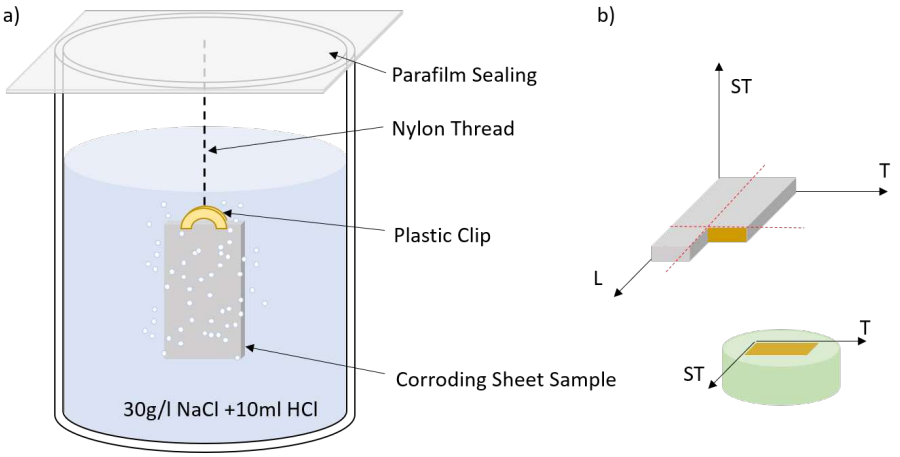


Figure 8: (a) Schematic experimental set up as previously used for IGC testing according to ISO EN 11846 method B. (b) Metallographic cross-section preparation sites dependent to analyze the penetration depth in longitudinal (L), transverse (T) and short-transverse (ST) directions.

then shielded from the environment with Parafilm® and placed in a water bath at a constant temperature of 25°C. Schematically, the set-up is visible in Fig. 8 a).

Following the immersion test, samples are rinsed in distilled water and dried.

Metallographic cross-sections of three samples per condition are then prepared. The penetration depth of the intergranular corrosion attack is measured in the ST x T plane (Fig. 8 b)) using optical light microscopy. The maximum penetration depth of each sample is calculated as the average of the five largest penetration depths. Microstructure characterization of the materials in T4 condition was performed by Barker etching samples of each sheet direction and taking images using a optical light microscope. The Barker etching was performed for 80 s at a potential of 20 V [49].

Data Availability Statement

The data generated for this study will be made available upon reasonable request to the first author or the corresponding author.

Code Availability Statement

The codes used to generate the results in this study will be made available upon reasonable request to the first author or the corresponding author.

Acknowledgements

The authors would like to acknowledge Stefanie Düker and Rahul Thomas Kurian for their support with the experimental work. Sandia National Laboratories is a multi-mission laboratory managed and operated by National Technology and Engineering Solutions of Sandia, LLC., a wholly owned subsidiary of Honeywell International, Inc., for the U.S. Department of Energy National Nuclear Security Administration under contract DE-NA0003525. This paper describes objective technical

results and analysis. Any subjective views or opinions that might be expressed in the paper do not necessarily represent the views of the U.S. Department of Energy or the United States Government.

Funding Declaration

Not applicable

Declaration of Competing Interests

The Authors declare no Competing Financial or Non-Financial Interests.

Author Contributions

David Montes de Oca Zapiain: Conceptualization, Data curation, Investigation, Methodology, Validation, Visualization, Writing – original draft, Writing – review and editing;

Christoph Altenbach: Conceptualization, Data curation, Investigation, Methodology, Validation, Writing – original draft, Writing - Review & Editing, Visualization

Laura Kopruch: Conceptualization, Data curation,Validation, Investigation, Writing - Review & Editing, Visualization

Ryan M. Katona: Conceptualization, Visualization, Writing – original draft, Writing – review and editing, Resources, Funding;

Aditya Venkatraman: Conceptualization, Methodology, Writing – review and editing;

Daniela Zander: Resources, Writing - Review & Editing

References

[1] Y.-C. Gao, B.-X. Dong, H.-Y. Yang, X.-Y. Yao, S.-L. Shu, J. Kang, J. Meng, C.-J. Luo, C.-G. Wang, K. Cao, J. Qiao, M. Zhu, F. Qiu, Q.-C. Jiang, Research progress, application and development of high performance 6000 series aluminum alloys for new energy vehicles, Journal of Materials Research and Technology 32 (2024) 1868–1900. doi:https://doi.org/10.1016/j.jmrt.2024.08.018.
URL https://www.sciencedirect.com/science/article/pii/S2238785424018088

[2] D. Zander, C. Schnatterer, C. Altenbach, V. Chaineux, Microstructural impact on intergranular corrosion and the mechanical properties of industrial drawn 6056 aluminum wires, Materials & Design 83 (2015) 49–59.

[3] C. Schnatterer, C. Altenbach, D. Zander, The effect of simulated in-service heat impact on the microstructure and corrosion properties of a high cu containing al-mg-si alloy, Materials and Corrosion 70 (7) (2019) 1205–1213.

[4] C. Schnatterer, Interkristalline Korrosion und Spannungsrisskorrosion von Al-Mg-Si-Cu-Drähten, Shaker Verlag, 2018.

[5] T. Avramenko, S. Michel, J. Kollender, I. Burda, U. Hans, C. Affolter, Review on environmentally assisted static and fatigue cracking of al-mg-si-(cu) alloys, Metals 14 (6) (2024) 621.
URL https://www.mdpi.com/2075-4701/14/6/621

[6] C. Altenbach, D. Zander, C. Schnater, R. Müller-Jena, T. Beyer, M. Rosefort, J. Becker, A. Stieben, T. Hentschel, Korrosionsmechanismen von aluminiumknetlegierungen, abhängigkeiten von legierungselementen und prozessen am beispiel der interkristallinen korrosion verstehen und prüfen, presentation at the ASMET Automobiltagung (2022).

[7] R. M. Katona, E. K. Karasz, R. F. Schaller, A review of the governing factors in pit to crack transitions of metallic structures, Corrosion 79 (1) (2023) 72–96. doi:10.5006/4179.

[8] R. Müller-Jena, J. Becker, T. Beyer, T. Hentschel, M. Rosefort, A. Stieben, D. Zander, The effect of deformation mode and microstructure on the igc susceptibility of al–mg–si–cu alloys for automotive applications, in: Light Metals 2020, Springer, 2020, pp. 352–361.

[9] R. Müller-Jena, H. J. Springer, B. D. Zander, Einfluss von Kalt-und Warmumformprozessen auf die lokalen Korrosionsmechanismen von Al-Mg-Si-Cu-Legierungen, Lehrstuhl für Korrosion und Korrosionsschutz, 2022.

[10] G. Svenningsen, M. H. Larsen, J. H. Nordlien, K. Nisancioglu, Effect of thermomechanical history on intergranular corrosion of extruded almgsi (cu) model alloy, Corrosion science 48 (12) (2006) 3969–3987.

[11] A. K. Bhattamishra, K. Lal, Influence of ageing on corrosion behaviour of al–mg–si alloys in chloride and acid media, International Journal of Materials Research 89 (11) (2021) 793–796.

[12] M. H. Larsen, J. C. Walmsley, O. Lunder, R. H. Mathiesen, K. Nisancioglu, Intergranular corrosion of copper-containing aa6xxx almgsi aluminum alloys, Journal of the Electrochemical Society 155 (11) (2008) C550.

[13] C. Schnatterer, A. Bulinger, D. Zander, Evaluating the intergranular corrosion susceptibility of al-mg-si-cu alloys using electrochemical methods, Materials and Corrosion 67 (12) (2016) 1308–1313.

[14] G. Svenningsen, J. E. Lein, A. Bjørgum, J. H. Nordlien, Y. Yu, K. Nisancioglu, Effect of low copper content and heat treatment on intergranular corrosion of model almgsi alloys, Corrosion science 48 (1) (2006) 226–242.

[15] J. Holmestad, M. Ervik, C. D. Marioara, J. C. Walmsley, Investigation of grain boundaries in an al-mg-si-cu alloy, in: Materials Science Forum, Vol. 794, Trans Tech Publ, 2014, pp. 951–956.

[16] M. H. Larsen, J. C. Walmsley, O. Lunder, K. Nisancioglu, Effect of excess silicon and small copper content on intergranular corrosion of 6000-series aluminum alloys, Journal of the electrochemical society 157 (2) (2009) C61.

[17] H. Li, P. Zhao, Z. Wang, Q. Mao, B. Fang, R. Song, Z. Zheng, The intergranular corrosion susceptibility of a heavily overaged al-mg-si-cu alloy, Corrosion Science 107 (2016) 113–122. doi:https://doi.org/10.1016/j.corsci.2016.02.025. URL https://www.sciencedirect.com/science/article/pii/S0010938X16300683

[18] A. Shi, B. Shaw, E. Sikora, The role of grain boundary regions in the localized

corrosion of a copper-free 6111-like aluminum alloy, Corrosion 61 (6) (2005) 534–547.

[19] A. Bhattamishra, K. Lal, Microstructural studies on the effect of si and cr on the intergranular corrosion in al-mg-si alloys, Materials Design 18 (1) (1997) 25–28.

[20] G. Svenningsen, M. H. Larsen, J. C. Walmsley, J. H. Nordlien, K. Nisancioglu, Effect of artificial aging on intergranular corrosion of extruded almgsi alloy with small cu content, Corrosion science 48 (6) (2006) 1528–1543.

[21] P. Adapala, T. Avey, Y. Yuan, M. L. Lim, G. Bhaskaran, S. Das, A. Luo, G. S. Frankel, Understanding the effect of microstructure and composition on localized corrosion susceptibility of 6xxx aluminum alloys, npj Materials Degradation 8 (1) (2024) 52.

[22] S. Kumari, S. Wenner, J. C. Walmsley, O. Lunder, K. Nisancioglu, Progress in understanding initiation of intergranular corrosion on aa6005 aluminum alloy with low copper content, Journal of The Electrochemical Society 166 (11) (2019) C3114–C3123.

[23] Y. Zou, Q. Liu, Z. Jia, Y. Xing, L. Ding, X. Wang, The intergranular corrosion behavior of 6000-series alloys with different mg/si and cu content, Applied Surface Science 405 (2017) 489–496.

[24] S. Kairy, P. Rometsch, C. Davies, N. Birbilis, On the intergranular corrosion

and hardness evolution of 6xxx series al alloys as a function of si: Mg ratio, cu content, and aging condition, Corrosion 73 (10) (2017) 1280–1295.

[25] S. K. Kairy, T. Alam, P. A. Rometsch, C. H. Davies, R. Banerjee, N. Birbilis, Understanding the origins of intergranular corrosion in copper-containing al-mg-si alloys, Metallurgical and Materials Transactions A 47 (2016) 985–989.

[26] K. ichi Ikeda, T. Takashita, R. Akiyoshi, S. Hata, H. Nakashima, K. Yamada, K. Kaneko, Effects of scandium and zirconium addition on recrystallization behavior of al–mg–si alloy, MATERIALS TRANSACTIONS 59 (4) (2018) 590–597. doi:10.2320/matertrans.L-M2018802.

[27] R. Guemini, A. Boubertakh, G. W. Lorimer, Study of the recrystallization process of almgsi alloys containing transition elements, Journal of alloys and compounds 486 (1-2) (2009) 451–457.

[28] I. A. Sari, G. Ozcelik, O. Yucel, Impact of v additions on the microstructure and mechanical properties of al-6xxx alloy, Canadian Metallurgical Quarterly 64 (4) (2025) 1886–1895.

[29] M. Cornejo, T. Hentschel, D. Koschel, C. Matthies, L. Peguet, M. Rosefort, C. Schnatterer, E. Szala, D. Zander, Intergranular corrosion testing of 6000 aluminum alloys, Materials and Corrosion 69 (5) (2018) 626–633.

[30] M. Cornejo, T. Hentschel, D. Koschel, C. Matthies, L. Peguet, M. Rosefort, C. Schnatterer, E. Szala, D. Zander, A comparison of accelerated corrosion

tests for the assessment of the intergranular corrosion susceptibility of bare 6000 aluminum sheets, Materials and Corrosion 70 (4) (2019) 623–632.

[31] D. I. für Normung e.V., Corrosion of metals and alloys - determination of resistance to intergranular corrosion of solution heat-treatable aluminium alloys (iso11846:1995) (2008).

[32] Y. LeCun, Y. Bengio, G. Hinton, Deep learning, nature 521 (7553) (2015) 436–444.

[33] D. M. de Oca Zapiain, D. Maestas, M. Roop, P. Noel, M. Melia, R. Katona, Accelerating fem-based corrosion predictions using machine learning, Journal of The Electrochemical Society 171 (1) (2024) 011504.

[34] A. Venkatraman, R. M. Katona, D. Maestas, M. Roop, P. Noell, D. Montes de Oca Zapiain, An active learning framework for the rapid assessment of galvanic corrosion, npj Materials Degradation 8 (1) (2024) 54.

[35] L. B. Coelho, D. Zhang, Y. Van Ingelgem, D. Steckelmacher, A. Nowé, H. Terryn, Reviewing machine learning of corrosion prediction in a data-oriented perspective, npj Materials Degradation 6 (1) (2022). doi:10.1038/s41529-022-00218-4.

[36] S. Ma, Y. Du, S. Wang, Y. Su, Application of machine learning in material corrosion research, Corrosion Reviews 0 (0) (2023). doi:10.1515/corrrev-2022-0089.

[37] J. Li, L. Ye, G. Zou, Y. Wang, Z. Yuan, J. Tang, Synergistic enhancement of strength and corrosion resistance in al-mg-si alloys through chemical composition design via machine learning approaches, Materials & Design (2025) 115310.

[38] X. Feng, Z. Wang, L. Jiang, F. Zhao, Z. Zhang, Simultaneous enhancement in mechanical and corrosion properties of al-mg-si alloys using machine learning, Journal of Materials Science & Technology 167 (2023) 1–13.

[39] S. Sheik, R. Mohammed, K. Teeparthi, Y. Raghuvamsi, Machine learning-based prediction of intergranular corrosion resistance in austenitic stainless steels exposed to various heat treatments, Journal of The Institution of Engineers (India): Series D 106 (1) (2025) 491–504.

[40] D. F. Falaakh, C. B. Bahn, Machine learning for modeling intergranular stress corrosion cracking of stainless steels in light water reactors with uncertainty quantification and explainability, npj Materials Degradation (2025).

[41] R. E. Schapire, et al., A brief introduction to boosting, in: Ijcai, Vol. 99, 1999, pp. 1401–1406.

[42] C. Schnatterer, D. Zander, Influence of the grain boundary chemistry on the intergranular corrosion mechanisms of a high-strength al-mg-si alloy, Surface and Interface Analysis 48 (8) (2016) 750–754.

[43] A. Venkatraman, R. M. Katona, D. M. de Oca Zapiain, Matse—multi-fidelity augmented time-series emulation: galvanic corrosion applications, Machine Learning: Science and Technology 6 (2) (2025) 025031.

[44] C. Williams, C. Rasmussen, Gaussian processes for regression, Advances in neural information processing systems 8 (1995).

[45] O. Kramer, Scikit-learn, in: Machine learning for evolution strategies, Springer, 2016, pp. 45–53.

[46] P. Goldberg, C. Williams, C. Bishop, Regression with input-dependent noise: A gaussian process treatment, Advances in neural information processing systems 10 (1997).

[47] Q. V. Le, A. J. Smola, S. Canu, Heteroscedastic gaussian process regression, in: Proceedings of the 22nd international conference on Machine learning, 2005, pp. 489–496.

[48] A. G. d. G. Matthews, M. Van Der Wilk, T. Nickson, K. Fujii, A. Boukouvalas, P. León-Villagrá, Z. Ghahramani, J. Hensman, Gpflow: A gaussian process library using tensorflow, Journal of Machine Learning Research 18 (40) (2017) 1–6.

[49] L. Barker, Revealing the grain structure of common aluminum alloy metallographic specimens, Trans. ASM 42 (1950) 347.

[50] F. Kahrıman, M. Zeren, Determination of activation energy for static recrystallization in al-mg-si alloys with different zr contents, Key Engineering Materials 951 (2023) 33–46.

[51] A. Lervik, S. Wenner, O. Lunder, C. Marioara, R. Holmestad, Grain boundary

structures and their correlation with intergranular corrosion in an extruded al-mg-si-cu alloy, Materials Characterization 170 (2020) 110695.

[52] G. S. Frankel, Pitting corrosion of metals. a review of the critical factors, Journal of The Electrochemical Society 145 (1998) 2186–2198. doi:10.1149/1.1838615.

[53] S. K. Kairy, P. A. Rometsch, K. Diao, J. F. Nie, C. H. J. Davies, N. Birbilis, Exploring the electrochemistry of 6xxx series aluminium alloys as a function of si to mg ratio, cu content, ageing conditions and microstructure, Electrochimica Acta 190 (2016) 92–103. doi:https://doi.org/10.1016/j.electacta.2015.12.098.
URL https://www.sciencedirect.com/science/article/pii/S0013468615310227

[54] K. D. Ralston, N. Birbilis, Effect of grain size on corrosion: A review, Corrosion 66 (7) (2010) 075005–1–075005–13. doi:10.5006/1.3462912.

[55] T. A. A. Inc., International alloy designations and chemical composition limits for wrought aluminum and wrought aluminum alloys (2025).

[56] L. Mondolfo, Structure and properties, Aluminum Alloys 518 (1976).

[57] D. Altenpohl, Aluminium und Aluminiumlegierungen, Springer Berlin Heidelberg: Berlin/Heidelberg, Germany, 1965.

[58] H. Zoller, A. Ried, Metallkundliche gesichtspunkte bei der entwicklung wenig abschreckempfindlicher almgsi-legierungen/metallurgical aspects in the develop-

ment of almgsi alloys with a low sensitivity to quenching, International Journal of Materials Research 62 (5) (1971) 354–358.